Microscopic Computer Simulations of Directional Coarsening in Face-centered Cubic Alloys

H. Gupta[1,2], R. Weinkamer[3,1,2], P. Fratzl[2], and J.L. Lebowitz[1]
[1] *Departments of Mathematics and Physics, Rutgers University, Busch Campus, New Brunswick, 08903 New Jersey, USA*
[2] *Erich Schmid Institut für Materialwissenschaft, Österreichische Akademie der Wissenschaften & Institut für Metallphysik. Montanuniversität Leoben, Jahnstraße 12, A-8700 Leoben, Austria*
[3] *Institut für Materialphysik der Universität Wien, Strudlhofgasse 4, A-1090 Wien, Austria*
(October 27, 2000)

We carried out Monte Carlo simulations of phase separation in a three-dimensional binary alloy with misfitting phases subjected to uniaxial external stress. A lattice of cylindrical or plate-like precipitates is formed at the mesoscale, as observed in real alloys. The rate of precipitate growth is much slower than the conventional $R(t) \sim t^{\frac{1}{3}}$ behavior in systems with no elastic misfit. Once a well-defined precipitate microstructure is formed, the reversal of external applied load has only a small effect.

Keywords: homogeneous phase transformations; nickel alloys; theory and modeling: thermodynamics, critical phenomena; rafting; computer simulation.

I. INTRODUCTION

The structural and mechanical properties of high-performance alloys are greatly influenced by the morphological arrangements of the different phases formed during phase separation following a quench from high temperature into the miscibility gap. A crucial factor controlling the composition and geometry of these phases at the mesoscale are coherent elastic strains between misfitting phases, e.g., between the γ and γ' phases in Ni-base superalloys [1,2]. The influence of such long-range elastic interactions on the morphology of a single coherent precipitate, the mutual arrangements of the precipitates and the coarsening kinetics of the microstructure has been investigated both experimentally and theoretically [3,4]. These studies found that the shape of the precipitates tends to be non-spherical, e.g. cuboidal [1,5–7], that the precipitates align themselves into regular arrays [8,9], and that their growth can be considerably slowed down compared to the case where there is no elastic stress [10,11]. The presence of an external stress during phase separation breaks the cubic symmetry and arrays of cylindrical precipitates parallel to, or plate-like precipitates perpendicular to the direction of external load are formed (directional coarsening or *rafting*) [12–18]. The type of topology depends on the signs of the external load (tensile or compressive) and of the misfit, and on the difference between the elastic constants in matrix and precipitates [19,20].

In this paper we use a conceptually simple microscopic model to study rafting in a face-centered cubic (fcc) binary alloy. This model has been used previously in two-dimensional simulations [14,20–22] where however the different types of precipitate microstructure (cylinders or plates) appear as striped patterns differing only in orientation. In the present three-dimensional simulations we observe regular arrays of cylindrical or plate-like precipitates, and the structure function reveals a higher degree of precipitate alignment than observed in two dimensions. Still, both the shape of the precipitates and their arrangement are far from perfect, with the mesoscopic lattice of the precipitates exhibiting the analog of defects found in atomic lattices, like dislocations or stacking-faults. The dynamics of these defects play an important role in the coarsening process [23].

The stability of the obtained microstructure was tested by reversal of the applied stress and was found fairly metastable in agreement with experiments. Another remarkable effect found in the simulations and known from some alloys with coherency strains, is a slowing down of the precipitate growth compared to the conventional $R(t) \propto t^{\frac{1}{3}}$ behavior holding for alloys with no elastic interactions [24].

II. THE MODEL

The model consists of a coherent *fcc* lattice with periodic boundary conditions and cubic lattice constant a, containing N atoms of two types - A and B - with radii R_A and R_B, $R_A > R_B$. The A atoms have a concentration $\bar{c} = N_A/N$, where N_A is the number of A atoms in the system. The associated spin variable $\gamma(\mathbf{r})$ at lattice site $\mathbf{r}$ takes the value $+1$ for an A atom and -1 for a B atom. The elastic forces due to the size mismatch between A and B atoms are modeled by connecting nearest neighbor atoms with springs [25], which can be compressed or stretched either

longitudinally or transversely. The three spring stiffnesses associated with these modes are L, T_1 and T_2 respectively. The addition of an external stress creates a homogeneous strain field $[\epsilon^0]$, such that the atom at site $\mathbf{r}$ is displaced by an amount $\epsilon^0.\mathbf{r} + \mathbf{v}(\mathbf{r})$, where $\mathbf{v}(\mathbf{r})$ is the displacement due to the compositional variations in the vicinity of the site $\mathbf{r}$. The uniformly stretched lattice is taken as a reference and all displacements $\mathbf{v}$ are measured with respect o it. The effect of this uniform extension or contraction of the reference lattice is to change the distances between nearest neighbors by a constant. In addition, at least a small elastic inhomogeneity between the A and B phases has to be present to include external stress effects in a nontrivial manner [20].

Under the assumption that the relaxation time of the lattice distortions is much smaller than the diffusion time of the atoms, and the homogeneous strain displacement is much larger than the displacements $\mathbf{v}(\mathbf{r})$, we can minimize the energy over the atomic displacements $\mathbf{v}$ [20,26,27,29]. The full elastic Hamiltonian may then be written as

$$\mathcal{H}_{el} = \frac{(R_A - R_B)^2}{2N} \sum_{\mathbf{k}} \Phi(\mathbf{k}) \mid \Gamma(\mathbf{k}) \mid^2 \tag{1}$$

where $\Gamma(\mathbf{k})$ is the Fourier transform of $\gamma(\mathbf{r})$, $\Gamma(\mathbf{k}) = \sum_{\mathbf{r}} \gamma(\mathbf{r}) e^{i\mathbf{k}.\mathbf{r}}$, and $(R_A - R_B)^2\Phi(\mathbf{k})$ is the elastic potential in Fourier space [20] (for the functional form of $\Phi(\mathbf{k})$ see equations (19) - (22) in the Appendix). Figure 1 shows two-dimensional cross sections of $\Phi(\mathbf{k})$ for tensile, compressive and zero stress. The potential is highly anisotropic, the cubic symmetry being broken by the application of external stress. In addition to the elastic interaction we also include a nearest neighbor "chemical" interaction $-J\gamma(\mathbf{r})\gamma(\mathbf{r}')$, chosen to induce phase separation ($J > 0$ and $\mathbf{r}.\mathbf{r}'$ are nearest neighbor lattice sites). The total Hamiltonian can be written in a form similar to equation (1)

$$\mathcal{H}_{tot} = \frac{1}{2N} \sum_{\mathbf{k}} \Psi(\mathbf{k}) \mid \Gamma(\mathbf{k}) \mid^2 = \frac{1}{2} \sum_{\mathbf{r},\mathbf{r}'} \psi(\mathbf{r} - \mathbf{r}')\gamma(\mathbf{r})\gamma(\mathbf{r}') \tag{2}$$

where the new $\Psi(\mathbf{k})$ is defined in equation (25) of the Appendix. The pairwise interaction $\psi(\mathbf{r} - \mathbf{r}')$ now includes both short range chemical as well as long range elastic interactions.

A. Numerical values

For our simulations we took an *fcc* lattice with 48^3 cubic unit cells, i.e., $N = 442368$. Two different concentrations of A atoms, $\bar{c} = 0.2$ and 0.5, were chosen. Given the Born-von Karman coupling constants $\{\Phi_{ij}^m\}$ parameterizing the experimental phonon dispersion curves of metals, the microscopic spring stiffnesses L, T_1, and T_2 are then determined by the following relations

$$\begin{aligned} L &= \Phi_{xx}^{[110]} + \Phi_{xy}^{[110]} \\ T_1 &= \Phi_{xx}^{[110]} - \Phi_{xy}^{[110]} \\ T_2 &= \Phi_{zz}^{[110]} \end{aligned} \tag{3}$$

For typical *fcc* metals (three are listed in Table 1), the longitudinal stiffness is an order of magnitude larger than the transverse stiffness. In principle, springs between further neighbors could also be considered, but normally the nearest neighbor coupling dominates [30], so we did not include this extra complication. For our simulations we used the Born-von Karman coupling constants for Cu. The long-wave relations between L, T_1, T_2 and the bulk elastic moduli c_{11}, c_{12} and c_{44} are [27]

$$\begin{aligned} ac_{11} &= 2L + 2T_1 \\ ac_{12} &= L - 3T_1 - 2T_2 \\ ac_{44} &= L + T_1 + 2T_2 \end{aligned} \tag{4}$$

Here a denotes the cubic lattice constant. Due to our parameter choice, the model has negative elastic anisotropy, i.e. $(c_{11} - c_{12} - 2c_{44})/c_{44} < 0$, which is found in metals like Al, Cu, Fe, and Ni, and the elastically soft directions are the cubic $\langle 100 \rangle$-axes [3].

The relative strength of the elastic and chemical interactions is given by the dimensionless "elastic misfit parameter" λ, which is defined for our model as

$$\lambda = \frac{(R_A - R_B)^2 L}{J} \tag{5}$$

λ is related to the lattice misfit $\delta \equiv (a_A - a_B)/a_A$, where a_A and a_B are the unstressed lattice constants for a pure A phase or B phase respectively, as $\lambda = \lambda_0 \delta^2 L/\sigma$ [22]. $\lambda_0 \approx 30$ is a dimensionless prefactor and σ is the interfacial energy. Assuming a typical value for $\sigma \approx 10^{-2} J m^{-2}$, $\lambda = 4.2$ corresponding to $\delta \approx 1$ % was chosen. Choosing a metal different from Cu in Table 1, results in just a slight change of the lattice misfit. To include uniaxial external stress, we chose $\alpha\epsilon^0_{11} = \pm 0.1$, with + for tensile and − for compressive stress (for the definition of α see Appendix, equation (18)), which results in lateral strains of $\epsilon^0_{22} = \epsilon^0_{33} \approx \mp 0.42\epsilon^0_{11}$. With these parameters for the lattice mismatch and elastic inhomogeneity the formation of cylindrical precipitates under tensile stress and plate-like precipitates under compressive stress was expected [19,20]. Simulations were carried out at a temperature $T = 5.0 J/k_B$ below the critical temperature $T_c \approx 12.5 J/k_B$ determined approximately from a series of MC runs (A mean-field calculation for the critical temperature, discussed below, gives a slightly higher value of $14 J/k_B$). No new features, compared to the simulations at lower $T = 5.0 J/k_B$, were observed in simulations at a higher $T = 8.0 J/k_B$ and are therefore not reported here. Atomic configurations on the lattice evolved by the Metropolis algorithm with Kawasaki exchange dynamics of nearest-neighbor atoms [28]. The time unit is one Monte Carlo step (MCS), i.e. one attempted exchange per site. Starting from a configuration of randomly distributed A and B atoms corresponding to the high-temperature phase of the alloy, the system was quenched into the miscibility gap, and annealed at fixed temperature for a maximum of 6000 MCS under compressive or tensile uniaxial load, and for comparison, without external load. In a second series of simulations, the system was evolved under a given load for 3000 MCS, at which point the load was reversed. The system evolved under the reversed load for another 3000 MCS.

B. Mean Field approximation

Following the approach in [21], the total mean field free energy of our model equals

$$F^{MF} = E^{MF} - TS^{MF} \approx F_0^{MF} + \frac{1}{2} \sum_{\mathbf{k} \neq \mathbf{0}} |\overline{\Gamma}(\mathbf{k})|^2 \left(\frac{k_B T}{4\bar{c}(1-\bar{c})} + \Psi(\mathbf{k}) - \psi(\mathbf{0}) \right) \tag{6}$$

where $\overline{\Gamma}(\mathbf{k}) \equiv \sum_{\mathbf{r}} e^{i\mathbf{k}\cdot\mathbf{r}} \overline{\gamma}(\mathbf{r})$ and $\overline{\gamma}(\mathbf{r})$ is the mean value of the occupation variable at $\mathbf{r}$, and F_0^{MF} depends only on $\bar{c}$. For large T the coefficient of $|\overline{\Gamma}(\mathbf{k})|^2$ is positive for all $\mathbf{k}$, so the uniform state ($\overline{\gamma}(\mathbf{r}) = 2\bar{c} - 1$, $\overline{\Gamma}(\mathbf{k}) = 0$ for $\mathbf{k} \neq 0$) is stable. As the temperature decreases, the coefficient of $|\overline{\Gamma}(\mathbf{k})|^2$ may become negative for some $\mathbf{k}^* \neq \mathbf{0}$, creating an instability in the system with concentration waves at $\mathbf{k}^*$. Since the maximum value of $1/4\bar{c}(1-\bar{c})$ is 1, for $\bar{c} = 1/2$, such an instability can occur if and only if $T < T_c^{MF}$, where

$$k_B T_c^{MF} = \max_{\mathbf{k} \neq \mathbf{0}} [\psi(\mathbf{0}) - \Psi(\mathbf{k})] \tag{7}$$

To show the dependence of T_c^{MF} on external stress, Figure 2 shows T_c^{MF} as a function of the homogeneous strain field arising from the external stress (i.e. as a function of $\alpha\epsilon^0_{11}$) at different values of the elastic misfit λ. The elastic misfit raises the critical temperature T_c^{MF}, but the increase is less for positive (tensile) stress than compressive stress. The difference between the tensile and compressive cases comes from the different structure of $\Phi(\mathbf{k})$ in Figure 1 for the two cases. The elastic potential $\Phi(\mathbf{k})$ under tensile and compressive stress appear identical and rotated by 90^o, but in fact the minima of the potential in the tensile case lies in two identical pairs of lobes along the two cubic axes perpendicular to the external stress axis, while it lies along a single pair of lobes along the stress axis in the compressive case. The difference in the nature and depth of the elastic minima in the tensile and compressive cases for the same absolute value of the external load parameter $\alpha\epsilon^0_{11}$ results in the asymmetry of the T_c^{MF} plot as a function of external stress.

III. RESULTS & DISCUSSION

A. Precipitate morphology

Figure 3 shows snapshots of the configurations with $\bar{c} = 0.2$ evolved at $k_B T/J = 5.0$ under tensile load, at 400 MCS, where the depicted box comprises about $\frac{1}{6}$ of the whole system. The figure on top shows schematically the

expected cylindrical precipitate morphology and their regular arrangement, and is subdivided into three vertical columns containing three cylinders each. For clarity, the cylinders in each vertical column are shown with different shades of grey. Following this subdivision, the snapshots (below) of the actual precipitate morphology show the whole box, but each vertical column of precipitates is plotted separately to avoid obstructing the view of precipitates in one column by the adjacent one. Sites occupied by A atoms are represented by cubes and sites occupied by B atoms are left empty. The form of the precipitates in the snapshots is roughly cylindrical with the axes aligned approximately along the direction of the external stress. These cylinders are far from perfect, some being incomplete, as in the leftmost figure, others connected to neighboring ones. Moreover, the cylinder axes wiggle along the direction of external stress with varying cross-sections. However, the cylindrical precipitates are quite regularly spaced and clearly aligned with respect to each other. This fairly regular, nearly periodic arrangement corresponds to a *meso-lattice*. Its dynamics and the effect on coarsening under applied load were investigated in [23].

In Figure 4, a similar plot shows the case of compressive stress. The figure on top shows schematically the plate-like precipitates aligned perpendicular to the external stress axis, forming a linear array of plates. Again, the real precipitates are far from perfectly homogeneous plates. In fact, while a sideways view (right bottom figure) shows precipitates arranged regularly along the stress axis, an oblique view (left bottom) shows that the precipitate structures are in fact highly fragmented parts of plates, which lie in a plane normal to the external stress axis.

B. Structure function

The time dependent structure function $S(\mathbf{k},t)$ of the precipitate microstructure

$$S(\mathbf{k},t) = \frac{1}{N} \mid \sum_{\mathbf{r}} e^{i\mathbf{k}.\mathbf{r}} \gamma(\mathbf{r},t) \mid^2 \equiv \frac{1}{N} \mid \Gamma(\mathbf{k},t) \mid^2 \tag{8}$$

can be directly compared with the results of small angle scattering experiments. The elastic misfit strain ($\lambda \neq 0$) arising from the different size of A and B atoms breaks the spherical symmetry of $S(\mathbf{k},t)$, producing a flower shaped pattern with branches along the reciprocal $\langle 100 \rangle$ directions. This has been shown in two-dimensional simulations [20,22] as well as in small-angle scattering experiments, e.g. for Ni-Al-Mo alloys [31].

Alloys under external load have shown a further symmetry breaking; the [100] direction corresponding to the external load direction behaves differently from the (normally equivalent) other $\langle 100 \rangle$ directions [33]. Figure 5 shows $S(\mathbf{k},t)$ for the case of tensile, zero, and compressive external stress simulations ($\bar{c} = 0.2$ and $T = 5.0 J/k_B$), at 4000 MCS. Under zero external stress (Figure 5, (B)), $S(\mathbf{k},t)$ has lobes of equal intensity along the $\langle 100 \rangle$ directions. Under tensile stress $S(\mathbf{k},t)$ is flattened from a three-dimensional to a two-dimensional structure, with lobes along the two axes normal to the external stress axis, and very little intensity parallel to it (Figure 5, (A)). When compressive stress is applied, the concentration inhomogeneity occurs almost exclusively along the external stress direction, resulting in a one-dimensional streak of intensity parallel to the [100] direction (Figure 5, (C)). In addition to changes in symmetry of $S(\mathbf{k},t)$ when compressive or tensile load is applied, there is another quite remarkable feature. Looking at Figure 5 (C), for instance, there is not just a single pair of lobes left and right of the origin at $\mathbf{k} = 0$. In fact, there is a whole series of lobes corresponding to several orders of diffraction from the parallel array of plates. This indicates a substantially higher degree of order in the arrangement of precipitates than the corresponding two-dimensional model [20,22] where only the first order appeared in $S(\mathbf{k},t)$. Figures 5 (A) and (B) allow similar conclusions for the precipitate arrangement under tensile and zero load. In all cases, the several lobes visible along the reciprocal $\langle 100 \rangle$ directions indicate a very high degree of ordering in the arrangement of precipitates. However, the two and three dimensional simulations are not exactly comparable, since no experimental data are available for the surface tension σ in two dimensions.

C. Anisotropy

In order to get a quantitative measure of the kinetics of symmetry breaking and precipitate formation, we defined two different parameters. The first is the *anisotropy* $\kappa(t)$ of the structure function $S(\mathbf{k},t)$, defined in the following way. Points in the Brillouin zone are partitioned into groups according to which of the 26 unit vector directions ($\langle 100 \rangle$, $\langle 110 \rangle$, or $\langle 111 \rangle$) they are closest to. The average value of the structure function in the $\langle 100 \rangle$ group is denoted

$\langle S(\mathbf{k},t)\rangle_{\langle 100\rangle}$, and the analog for the remaining off-axis directions is $\langle S(\mathbf{k},t)\rangle_{\langle 110\rangle\cup\langle 111\rangle}$. The anisotropy $\kappa(t)$ is then defined as

$$\kappa(t) = \frac{\langle S(\mathbf{k},t)\rangle_{\langle 100\rangle} - \langle S(\mathbf{k},t)\rangle_{\langle 110\rangle\cup\langle 111\rangle}}{\langle S(\mathbf{k},t)\rangle_{\langle 100\rangle} + \langle S(\mathbf{k},t)\rangle_{\langle 110\rangle\cup\langle 111\rangle}} \tag{9}$$

$\kappa(t)$ is 0 for a random or spherically symmetric configuration, and 1 when $S(\mathbf{k},t)$ is nonzero only along the $\langle 100\rangle$ directions. Figure 6 shows the behavior of $\kappa(t)$ on the time scale $t^{\frac{1}{3}}$ for both concentrations, starting from a random configuration up to 6000 MCS. Starting from the expected value of $\kappa(t=0) \sim 0$ for a random configuration, $\kappa(t)$ increases smoothly for tensile, compressive and zero external stresses to approximately 0.75 by 6000 MCS. The evolution of $\kappa(t)$ is basically similar for different external stress conditions, and the overlap of the $\kappa(t)$ plots for different conditions of external load is greater for $\bar{c} = 0.5$. The main conclusion from this analysis is that the degree of alignment of the precipitates along $\langle 100\rangle$ directions, as defined by $\kappa(t)$, is controlled by the anisotropy of the elastic misfit (i.e., the value of λ) but not by the direction and amount of external stress (i.e., $\alpha\epsilon^0_{11}$). This is in agreement with previous results in two dimensions [14,20,22]. Also in agreement with the 2-D case, we observe higher values of $\kappa(t)$ for $\bar{c} = 0.5$ than for $\bar{c} = 0.2$, corresponding to a more pronounced alignment of the domains at the higher concentration.

The inset in the left subfigure of Figure 6 shows the effect of reversal of load direction (filled symbols) after 3000 MCS. For the compressive case, $\kappa(t)$ decreases by about 15 % over a period of 10^3 MCS. In contrast, $\kappa(t)$ for the tensile configuration initially decreases by only 5 %, and starts increasing very slowly by 6000 MCS. All these changes are rather small, probably because $\kappa(t)$ is not much influenced by external load, as already mentioned.

D. Asymmetry

Since the anisotropy does not provide insight into the symmetry breaking induced by external load or the stability of the microstructure to changes in load, we define a second parameter, the *asymmetry* $\eta_{[100]}(t)$ along the [100] direction as

$$\eta_{[100]}(t) = \frac{\langle S(\mathbf{k},t)\rangle_{[100]}}{\langle S(\mathbf{k},t)\rangle_{[100]} + \langle S(\mathbf{k},t)\rangle_{[010]} + \langle S(\mathbf{k},t)\rangle_{[001]}} \tag{10}$$

and analogously for the [010] and [001] directions. Now the angular brackets denote averaging over the [100] direction only. In Figure 7, the time evolution of the asymmetry components is plotted for $\bar{c} = 0.2$ and 0.5. The component parallel to the external stress axis are marked by '+' in the symbols. For compressive load along the [100], $\eta_{[100]}(t)$ approaches 1 and both other components go to 0 as time increases. For tensile stress, the two components normal to the load axis increase and the parallel component decreases. The two components perpendicular to the load axis are not equal, but this difference is probably a spontaneous symmetry breaking occurring in a random fashion, as can be reasoned from the cross over of these perpendicular components for $\bar{c} = 0.5$ at $\sim$ 2000 MCS. For zero load, a symmetry breaking is also observed. For high concentration ($\bar{c} = 0.5$), the magnitude of this splitting is quite large, i.e., even when no external stress is applied, precipitates can join together locally, forming a microstructure similar to those observed in samples annealed under external load, with the difference that the orientation of the precipitates varies across the specimen. Similar effects have also been found in experiments [33]. Clearly, the symmetry breaking induced by external load occurs much earlier ($\sim$ 10 MCS) and is much larger compared to the case of no load ($\sim$ 500 MCS).

The inset figures (again, filled symbols) at $\bar{c} = 0.2$ shows the effect of reversing the external stress direction at 3000 MCS. On changing the load from compressive to tensile, the asymmetry parallel to the load axis decreases, and the components perpendicular to the stress increase, with a rate approximately half of the decrease of the parallel component. On changing from tensile to compressive load, the effects are much smaller; the parallel component of the load increases only slightly after the change. Generally speaking, the reversal of external load has only a small effect on the domain structure. Certainly, the parallel cylinder morphology is not transformed into an arrangement of parallel plates or vice-versa during the simulations. This indicates that the arrangements obtained after symmetry breaking are fairly metastable. This is not surprising since the intermediate structures that would have to form in the transformation from cylinders to plates perpendicular to the cylinder axis (or vice versa) would correspond to higher elastic energies. Similar effects are observed in experiments on Ni-base alloys [34], in which pre-strained alloys evolved under stress-free conditions showed rafted morphologies similar to those obtained by annealing under external stress. The effects in [34] were interpreted on the basis of misfit dislocations, which are excluded in the present model.

E. Precipitate Size and Coarsening

The typical size of precipitates can be estimated from the total interface present in the system. For coherent precipitates of A atoms embedded in a matrix of B atoms, the total number of A-B bonds N_{AB} can be related to the amount of interface between precipitates and matrix. N_{AB} is given by

$$N_{AB} = \frac{1}{2} \sum_{\mathbf{r}} \sum_{i=1}^{6} [1 - \gamma(\mathbf{r})\gamma(\mathbf{r} + \mathbf{a}_i)] \tag{11}$$

where the vectors $\mathbf{a}_i$, defined at the beginning of the Appendix, connect the site $\mathbf{r}$ with its nearest neighbors. We define an average linear dimension of the precipitates by $R_s \equiv \frac{6V}{S}$ where V and S are the total volume and surface of the domains. For cubic precipitates, R_s would just be their edge length. If we assume that the interfaces are $\{100\}$ planes, then each surface atom has 4 AB bonds and corresponds to an area of $a^2/2$ and $S = N_{AB}a^2/8$. For an alloy with composition $\bar{c}$, $V = N\bar{c}a^3/4$, which leads us to the expression

$$R_s = \frac{12N\bar{c}}{N_{AB}}a \tag{12}$$

A plot of $R_s(t)$ versus $t^{\frac{1}{3}}$ is given in Figure 8. For comparison, the solid line represents the mean precipitate size for a *fcc* Ising model at the same values of T/T_c, when elastic effects are neglected. Typical precipitate sizes are smaller for lower concentrations due to a higher supersaturation of solute (A) atoms in the matrix (B) phase. The Lifshitz-Slyozov-Wagner (LSW) theory [24] predicts that in the absence of elastic interactions, the precipitate size $R(t)$ follows a power law $R(t) \sim t^{\frac{1}{3}}$, which is certainly not the case for our simulations.

Several striking features are visible in Figure 8. First, R_s evolves in a very similar way, regardless of whether external load is applied or not, and completely differently from the Ising model with no elastic misfit interactions. The insensitivity of R_s to external stress is similar to what was found in two dimensions [14,20]. What is completely different, however, is that the growth of R_s cannot be described by a law of the type $R_s \approx R_s^0 + (Dt)^{\frac{1}{3}}$ as found in the 2-D case. After about 600 MCS (when the precipitate structure has fully developed), the growth of R_s is considerably slowed down and - at $\bar{c} = 0.5$ - it almost comes to a stand-still. In contrast, R_s for the Ising model grows nearly linearly in $t^{\frac{1}{3}}$ after about 1000 MCS, consistent with much theoretical and simulation work [37–40] on the kinetics of phase separation and precipitate growth for alloys where the only driving force for coarsening is the reduction of surface energy.

At this time, we can only speculate about the possible origin of the slowing down in the presence of elastic interactions. First, finite size effects cannot be completely excluded. Though R_s is always much smaller than the system size (by about a factor of 4), the cylindrical or plate-like precipitates extend practically to infinity considering the periodic boundary conditions, which can cause a stabilizing effect. In addition, it becomes energetically favourable for the spacing between precipitate rows or columns to be an integral fraction of the system size, to maintain the same spacing between precipitate row or columns in adjacent simulation cells. This may hinder the coarsening process if the number of rows or columns is small. To check the effect the finite size of the system has on our results, we have performed simulations at smaller system sizes with 32^3 unit cells, i.e 131072 atoms. We find no difference in the magnitude of the slowing down of coarsening or the time at which it starts becoming significant. The most likely explanation for the slow coarsening, however, is the highly ordered arrangement of precipitates found in the present simulations. As clearly visible in $S(\mathbf{k}, t)$ (see subsection III B), the alignment of precipitates is much more pronounced in 3-D than in 2-D, and it is probable that the third dimension favors a higher degree of alignment. Periodic arrangements of cylinders or plates are, however, quite resistant to coarsening since an increase in domain size must be accompanied by an increase in the spacing between domains which is not possible continuously if the precipitates are arranged on a lattice. In fact, the mechanisms by which coarsening can proceed is the movement of defects, like the analogs of dislocations, interstitials and vacancies, in the mesoscopic lattice of precipitates [23]. It is not surprising that this leads to a slower coarsening process [10,11] than in alloys where precipitates are randomly distributed.

To compare with experimental results on the anisotropy for Ni-base superalloys, we also looked at how the anisotropy κ varies as a function of R_s. The results are plotted in Fig. 9 for low ($\bar{c} = 0.2$) and high ($\bar{c} = 0.5$) concentration of A atoms. For the lower concentration of A atoms, κ varies almost linearly for small values of R_s. An experimental study of the variation of κ as a function of R_s in Ni-base superalloys showed a similar behavior [31].

IV. CONCLUSION

We have studied a fully microscopic model for phase separation and rafting in three dimensions in a binary alloy with misfitting phases leading to long ranged coherent elastic strains. The internal coherency strains and external homogeneous stresses applied during phase separation are found to have a dramatic effect on the precipitate morphology and the topology of the microstructure. It is very surprising that despite the complete neglect of dislocations and plasticity effects in our model, which are always present in directional coarsening [32,33], our rafted precipitate morphologies bear a striking resemblance to the experimental X-ray scattering and transmission electron microscopy data on materials like the Ni-base alloys. The main results of our investigations are as follows:

- Depending on the product of the sign of the external uniaxial stress and lattice inhomogeneity (i.e., on the sign of $\alpha\epsilon^0_{11}$), the precipitate morphology consists of an array of plate-like precipitates perpendicular to or cylindrical precipitates parallel to the external stress axis. These structures are, however, far from perfect [23].

- The structure function shows both the breaking of spherical symmetry due to elastic interactions as well as the breaking of cubic symmetry due to the application of external stress, as observed in experiments [31,33]. However, a higher degree of alignment of precipitates is observed in our three dimensional precipitate morphologies in comparison with simulations on a similar system in two dimensions [20,22].

- The anisotropy of the structure function behaves as found in the two-dimensional simulations [20,22] i.e., it is strongly affected by the elastic misfit but only weakly by the external load. The breaking of cubic symmetry due to the application of external stress is described by the asymmetry of the structure function, which shows that after symmetry breaking, the precipitate microstructure is resistant against load reversal. This bears some similarities with the stress-free evolution behavior of pre-strained Ni-base alloys [34], which were, however, explained on the basis of misfit dislocations.

- Domain growth slows down considerably from the power law $R_s(t) \sim t^{\frac{1}{3}}$ observed in the two-dimensional simulations [20,22]. It is possible that the high degree of alignment seen in three dimensions stabilizes the microstructure against coarsening. The slowing down of precipitate growth from a $R_s(t) \sim t^{\frac{1}{3}}$ behavior has been observed experimentally, for example in Ni-Cu-Si [35] and Ti-Mo alloys [36].

V. ACKNOWLEDGMENTS

We thank O. Penrose, A. Khachaturyan, O. Paris, and T. Tsakalakos for useful discussions. This work was supported by NSF Grant No. NSF-DMR-9813268 and Air Force Grant number AFOSR F49620-98-1-0207.

---

[1] Maheshwari, A. and Ardell, A. J., *Phys. Rev. Lett.*, 1993, **70**, 2305.

[2] Calderon, H. and Kostorz, G., in *Neutron Scattering in Materials Science*, eds. S. M. Shapiro, S. C. Moss, and S. D. Jorgensen, Mat. Res. Soc. Symp. Proc. 166, Materials Research Society, Pittsburgh, 1990.

[3] For a review, see Fratzl, P., Penrose, O. and Lebowitz, J. L., *J. Stat. Phys.*, 1999, **95**, 1429.

[4] Orlikowski, D., Sagui, C., Somoza, A., and Roland, C., *Phys. Rev. B*, 1998, **59**, 8646.

[5] Thompson, M. E. and Voorhees, P. W., *Acta mater.*, 1999, **47**, 983.

[6] Wang, Y. and Khachaturyan, A. G., *Acta metall. mater.*, 1995, **43**, 1837.

[7] Rubin, G. and Khachaturyan, A. G., *Acta mater.*, 1999, **47**, 1995.

[8] Koyama, T. and Miyazaki, T., *Mater. JIM*, 1998, **39**, 169.

[9] Wang, Y., Chen, L.-Q. and Khachaturyan, A. G., *Acta metall. mater.*, 1993, **41**, 279.

[10] Miyazaki, T. and Doi, M., *Mater. Sci. Engg.*, 1989, **A110**, 175.

[11] Onuki, A. and Nishimori, H., *Phys. Rev. B*, 1991, **43**, 13649.

[12] Tien, J. K. and Copley, S. M., *Metall. Trans.*, 1971, **2**, 215.

[13] Chang, J. C. and Allen, S. M., *J. Mater. Res.*, 1991, **6**, 1843.

[14] Laberge, C. A., Fratzl, P. and Lebowitz, J. L., *Phys. Rev. Lett.*, 1995, **75**, 4448.

[15] Lee, J. K., *Mater. Sci. Engg.*, 1997, **A238**, 1.

[16] Li, D. Y. and Chen, L. Q., *Scripta mater.*, 1997, **37**, 1271.

[17] Li, D. Y. and Chen, L. Q., *Acta mater.*, 1999, **47**, 247.

[18] Hort, W. and Johnson, W. C., *Metallurgical and Materials Transactions*, 1996, **27A**, 1461.

[19] Socrate, S. and Parks, D. M., *Acta metall. mater.*, 1993, **41**, 2185.

[20] Laberge, C. A., Fratzl, P. and Lebowitz, J. L., *Acta mater.*, 1997, **45**, 3949.

[21] Fratzl, P. and Penrose, O., *Acta metall. mater.*, 1995, **43**, 2921.

[22] Fratzl, P. and Penrose, O., *Acta mater.*, 1996, **44**, 3227.

[23] Weinkamer, R., Gupta, H., Fratzl, P., and Lebowitz, J. L., submitted to *Europhys. Lett.*.

[24] Lifshitz, I. M., and Slyozov, V. V., *J. Phys. Chem. Solids*, 1961, **19**, 35; Wagner, C., *Z. Elektrochem.*, 1961, **65**, 581.

[25] Born, M. and Huang, K., *Dynamical Theory of Crystal Lattices*, Oxford University Press, Oxford, 1954.

[26] Khachaturyan, A. G., *Soviet Phys. Crystallogr.*, 1965, **10**, 248.

[27] Cook, H. E. and DeFontaine, D., *Acta metall.*, 1969, **17**, 915; 1970, **18**, 189; 1971, **19**, 607.

[28] Binder, K. and Heermann, D. W., *Monte Carlo Simulation in Statistical Physics - An Introduction*, Springer, Berlin, 1988.

[29] Khachaturyan, A. G., *Theory of Structural Transformations in Solids*, Wiley, New York, 1983.

[30] Dederichs, P. H. and Schober, H., in *Landolt-Börnstein III/13a*, Springer, Berlin, 1981.

[31] Paris, O., Fährmann, M. and Fratzl, P., *Phys. Rev. Lett.*, 1995, **75**, 3458.

[32] Matan, N., Cox, D. C., Rae, C. M. F. and Reed, R. C., *Acta mater.*, 1999, **47**, 2031.

[33] Paris, O., Fährmann, M., Fährmann, E., Pollock, T. M. and Fratzl, P., *Acta mater.*, 1997, **45**, 1085.

[34] Fährmann, M., Fährmann, E., Paris, O., Fratzl, P. and Pollock, T. M., in *Superalloys 1996*, eds. R. D. Kissinger, D. J. Deye, D. L. Anton, A. D. Cetel, M. V. Nathal, T. M. Pollock, and D. A. Woodford, The Minerals, Metals & Materials

Society, 1996.

[35] Yoshida, S., Fukaya, M. and Miyazaki, T., *J. Japan Inst. Metals*, 1987, **51**, 18.

[36] Langmayr, F., Fratzl, P., and Vogl, G., *Phys. Rev. B*, 1994, **49**, 11759.

[37] See article by K. Binder in *Materials Science and Technology*, eds. P. Haasen, Vol. 5, Chapter 7, VCH, Weinheim, 1991.

[38] Gunton, J. D., San Miguel, M. and Sahni, P. S., in *Phase Transitions and Critical Phenomena*, eds. C. Domb and J. L. Lebowitz, Vol. 8, Academic Press, New York, 1983.

[39] Wagner, R. and Kampmann, R., in *Phase Transformations in Materials*, eds. P. Haasen, Vol. 5, Chapter 4, VCH, Weinheim. 1991.

[40] Furukawa, H., *Adv. Phys.*, 1985, **34**, 703.

VI. APPENDIX

Given a harmonic coupling between neighboring atoms on an *fcc* lattice, interactions with only half of the nearest neighbors have to be considered since a spring always connects two atoms. For an atom near the lattice site $\mathbf{r}$, the neighbors are indexed by i, $\mathbf{r}+\mathbf{a}_i$ being the position of the neighboring site, where

$$\mathbf{a}_1 = \frac{a}{2}\begin{pmatrix}1\\1\\0\end{pmatrix}, \mathbf{a}_2 = \frac{a}{2}\begin{pmatrix}0\\1\\1\end{pmatrix}, \mathbf{a}_3 = \frac{a}{2}\begin{pmatrix}1\\0\\1\end{pmatrix},$$

$$\mathbf{a}_4 = \frac{a}{2}\begin{pmatrix}1\\-1\\0\end{pmatrix}, \mathbf{a}_5 = \frac{a}{2}\begin{pmatrix}0\\1\\-1\end{pmatrix}, \mathbf{a}_6 = \frac{a}{2}\begin{pmatrix}-1\\0\\1\end{pmatrix}.$$

The distortion caused by the different sizes of atoms is measured by $\eta(\mathbf{r})$,

$$\eta(\mathbf{r}) = \frac{1}{2}(R_A - R_B)[\gamma(\mathbf{r}) - (2\bar{c}-1)], \tag{13}$$

where the constant term makes the average value of $\eta(\mathbf{r})$ over the whole lattice zero. The following abbreviations are useful

$$\eta^{(i)}(\mathbf{r}) = \eta(\mathbf{r}+\mathbf{a}_i) + \eta(\mathbf{r}), \tag{14}$$

$$\Delta v_j^{(i)}(\mathbf{r}) = v_j(\mathbf{r}+\mathbf{a}_i) - v_j(\mathbf{r}), \tag{15}$$

with $v_j(\mathbf{r})$ being the Cartesian components of $\mathbf{v}$. The elastic Hamiltonian $\mathcal{H}_{el}$, for the case of zero external load, is then

$$\mathcal{H}_{el} = \frac{1}{2}L\sum_{\mathbf{r}}\sum_{i=1}^{6}\{\frac{1}{2}[\Delta v_i^{(i)}(\mathbf{r}) + \mu\Delta v_{i+1}^{(i)}(\mathbf{r})]^2 - \sqrt{2}[\Delta v_i^{(i)}(\mathbf{r}) + \mu\Delta v_{i+1}^{(i)}(\mathbf{r})][\eta^{(i)}(\mathbf{r})] + [\eta^{(i)}(\mathbf{r})]^2\}$$
$$+\frac{1}{2}T_1\sum_{\mathbf{r}}\sum_{i=1}^{6}\frac{1}{2}[\Delta v_i^{(i)}(\mathbf{r}) - \mu\Delta v_{i+1}^{(i)}(\mathbf{r})]^2 + \frac{1}{2}T_2\sum_{\mathbf{r}}\sum_{i=1}^{6}[\Delta v_{i+2}^{(i)}(\mathbf{r})]^2, \tag{16}$$

where the indices here and in the equations below have to be taken modulo 3 and μ is defined as

$$\mu = \begin{cases} 1 & ,i = 1,2,3 \\ -1 & ,i = 4,5,6 \end{cases} \tag{17}$$

As shown in [20]. if a constant external stress is present, the internal and external strains are coupled only when the elastic moduli are taken inhomogeneous and composition dependent, while for homogeneous elastic moduli the external stress modifies the Hamiltonian only by the addition of a constant term. Hence, the longitudinal spring stiffness L coupling atoms at sites $\mathbf{r}$ and $\mathbf{r}+\mathbf{a}_i$ is made weakly dependent on the local atomic configuration in the following way

$$L(\alpha;\eta(\mathbf{r}),\eta(\mathbf{r}+\mathbf{a}_i)) = L(1+\alpha\eta^{(i)}(\mathbf{r})) \tag{18}$$

where $\alpha(R_A - R_B) \ll 1$ (weak coupling). On minimizing the elastic energy with respect to the atomic displacements $\mathbf{v}$, $\mathcal{H}_{el}$ takes the form of equation (1) where the elastic potential in Fourier space $\Phi(\mathbf{k})$ is given by

$$\Phi(\mathbf{k}) = \Omega(\mathbf{k}) - \sum_{i,j=1}^{3} G_i(\mathbf{k})\mathcal{D}_{ij}^{-1}(\mathbf{k})G_j^*(\mathbf{k}) \tag{19}$$

where the different terms are

$$\Omega(\mathbf{k}) = L\left\{3 - \sqrt{2}a\alpha\sum_{i=1}^{3}\epsilon_{ii}^0 + \sum_{i=1}^{3}\left[1 - \frac{1}{\sqrt{2}}a\alpha\left(\epsilon_{ii}^0 + \epsilon_{i+1i+1}^0\right)\right]c_ic_{i+1} + \sqrt{2}a\alpha\sum_{i=1}^{3}\epsilon_{ii+1}^0 s_is_{i+1}\right\} \tag{20}$$

$$G_i(\mathbf{k}) = \imath L\sum_{j\neq i}^{3}\left\{\left[-\sqrt{2} + \frac{1}{2}a\alpha\left(\epsilon_{jj}^0 + \epsilon_{ii}^0\right)\right]s_ic_j + a\alpha\epsilon_{ij}^0 c_is_j\right\} \tag{21}$$

$$\mathcal{D}_{ij}(\mathbf{k}) = \delta_{ij}\left\{2\left(L+T_1\right)\left[2 - c_i\left(c_{i+1}+c_{i+2}\right)\right] + 4T_2\left(1 - c_{i+1}c_{i+2}\right)\right\} + \left(1-\delta_{ij}\right)\left\{2\left(L-T_1\right)s_is_j\right\} \tag{22}$$

with $s_i \equiv \sin\left(\frac{k_ia}{2}\right)$, $c_i \equiv \cos\left(\frac{k_ia}{2}\right)$.

Inclusion of a nearest neighbor ferromagnetic Ising-type interaction between nearest neighbor atoms leads to an additional "chemical" term $\mathcal{H}_{ch}$ in the Hamiltonian for the system.

$$\mathcal{H}_{ch} = -J\sum_{\mathbf{r}}\sum_{i=1}^{6}\gamma(\mathbf{r})\gamma(\mathbf{r}+\mathbf{a}_i), \qquad J>0 \tag{23}$$

The total Hamiltonian for the system is then

$$\mathcal{H}_{tot} = \mathcal{H}_{el} + \mathcal{H}_{ch} = \frac{1}{2N}\sum_{\mathbf{k}}\Psi(\mathbf{k}) \mid \Gamma(\mathbf{k}) \mid^2 \tag{24}$$

where

$$\Psi(\mathbf{k}) = (R_A - R_B)^2\Phi(\mathbf{k}) - 4J\sum_{i=1}^{3}c_ic_{i+1}. \tag{25}$$

which can be written in real space as a pairwise interaction Hamiltonian

$$\mathcal{H}_{tot} \equiv \frac{1}{2}\sum_{\mathbf{r},\mathbf{r}'}\psi(\mathbf{r}-\mathbf{r}')\gamma(\mathbf{r})\gamma(\mathbf{r}') \tag{26}$$

with $\psi(\mathbf{r}) \equiv \frac{1}{N}\sum_{\mathbf{k}}\Psi(\mathbf{k})e^{-i\mathbf{k}.\mathbf{r}}$, and the sum over $\mathbf{r}$ and $\mathbf{r}'$ taken over all lattice sites.

	Cu	Al	Ni
$\Phi_{xx}^{[110]}$	13.1	9.8	17.3
$\Phi_{xy}^{[110]}$	14.8	11.4	19.1
$\Phi_{zz}^{[110]}$	-1.4	-1.6	-0.4
L	27.9	21.2	36.4
T_1	-1.7	-1.6	-1.8
T_2	-1.4	-1.6	-0.4

Table 1: Born-von Karman parameters Φ_{ij}^m and spring stiffnesses L, T_1, T_2 for three different *fcc* metals at room temperature [30], in units of N.m^{-1}.

FIGURE CAPTIONS

FIG. 1. Plots of two-dimensional cross sections of the interaction potential $\Phi(\mathbf{k})$ in the (001) plane, with lighter regions indicating regions of larger elastic potential. The external stress along the [100] axis breaks the cubic symmetry, with the minima of the elastic potential lying along the external stress axis for the compressive case and perpendicular to it for the tensile case. The horizontal axis corresponds to the direction of applied stress ([100]).

FIG. 2. Variation of the mean field critical temperature $T_c^{MF}(\lambda, \alpha\epsilon_{11}^0)$. The increase in T_c^{MF} with nonzero stress is asymmetric about zero, with a larger increase for negative (compressive) stress.

FIG. 3. Snapshots of the precipitate configuration for an alloy evolved from a random configuration at 4000 MCS for external tensile stress ($\bar{c} = 0.2$ and $T = 5.0J/k_B$). Lattice sites occupied by A atoms are represented by cubes (A atoms in the matrix are neglected), and sites containing B atoms are left empty. The schematic figure on top shows the direction of external stress, and divides the box into vertical columns each containing a column of three cylindrical precipitates. For clarity, each vertical column of precipitates is colored a different shade of grey, with the nearest column shown the darkest. In the three sub-figures showing the actual morphology, each column is pictured separately to avoid obscuring precipitates in the columns further back.

FIG. 4. Snapshots of the precipitate configuration for an alloy evolved from a random configuration at 4000 MCS for external compressive stress ($\bar{c} = 0.2$ and $T = 5.0J/k_B$). The schematic figure on top indicates the formation of plate-like precipitates normal to the external stress axis (indicated), and the right sub-figure views the precipitates at right angles to the stress axis, showing their regular arrangement along the axis. The left sub-figure shows the same configuration viewed at an oblique angle, showing the fragmented nature of the plates.

FIG. 5. Three-dimensional plot of structure function $S(\mathbf{k}, t)$ ($\bar{c} = 0.2$ and $T = 5.0J/k_B$) for tensile, zero, and compressive stress simulations at 4000 MCS, showing points with $S(\mathbf{k}, t) \geq 120.0$ as cuboids, the remaining sites being left empty. The anisotropic leaf-like structure is due to the elastic anisotropy, the breaking of the cubic symmetry due to the external stress.

FIG. 6. Time evolution of $\kappa(t)$ on a $t^{\frac{1}{3}}$ scale for $\bar{c} = 0.2$ (left) and $\bar{c} = 0.5$ (right) at $T = 5.0J/k_B$. Tensile ($\Box$), compressive ($\bigcirc$) and zero external stress ($\triangle$) are shown by different symbols. The inset figure in the $\bar{c} = 0.2$ plot shows the behavior on reversal of external stress direction (filled symbols). Both curves show a decrease, but the magnitude of the change is larger for the compressive $\rightarrow$ tensile case than in the tensile $\rightarrow$ compressive case.

FIG. 7. Time evolution of $\eta_i(t)$ on a $t^{\frac{1}{3}}$ scale for $\bar{c} = 0.2$ (left) and $\bar{c} = 0.5$ (right) at $T = 5.0J/k_B$. The component parallel to the external stress axis is denoted by a '+' sign in the symbol. Inset figures in the left column show the behavior on reversal of external stress (filled symbols). In the tensile $\rightarrow$ compressive case the larger component of the asymmetry perpendicular to the external stress axis continues to increase with the same rate after reversal of external stress direction.

FIG. 8. Time evolution of $R_s(t)$ on a $t^{\frac{1}{3}}$ scale. Tensile ($\Box$), compressive ($\bigcirc$) and zero external stress ($\triangle$) are plotted on the same graph for fixed concentration and temperature $T = 5.0J/k_B$. The solid line shows $R_s(t)$ for a nearest neighbor ferromagnetic Ising model on an *fcc* lattice.

FIG. 9. The anisotropy κ is shown as a function of precipitate size R_s. for tensile ($\square$), compressive ($\bigcirc$) and zero external stress ($\triangle$) on the same plot for low ($\bar{c} = 0.2$) and high ($\bar{c} = 0.5$) concentrations of A atoms.

FIG. 1

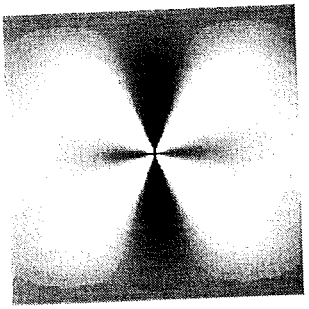

TENSILE

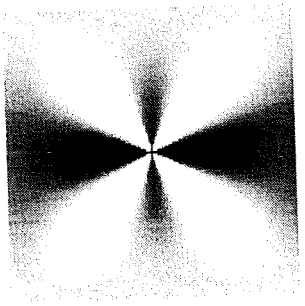

COMPRESSIVE

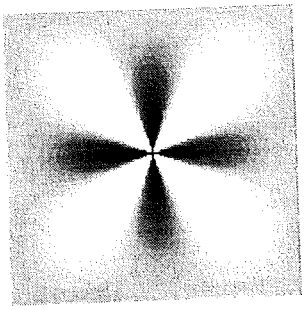

NO STRESS

FIG. 2

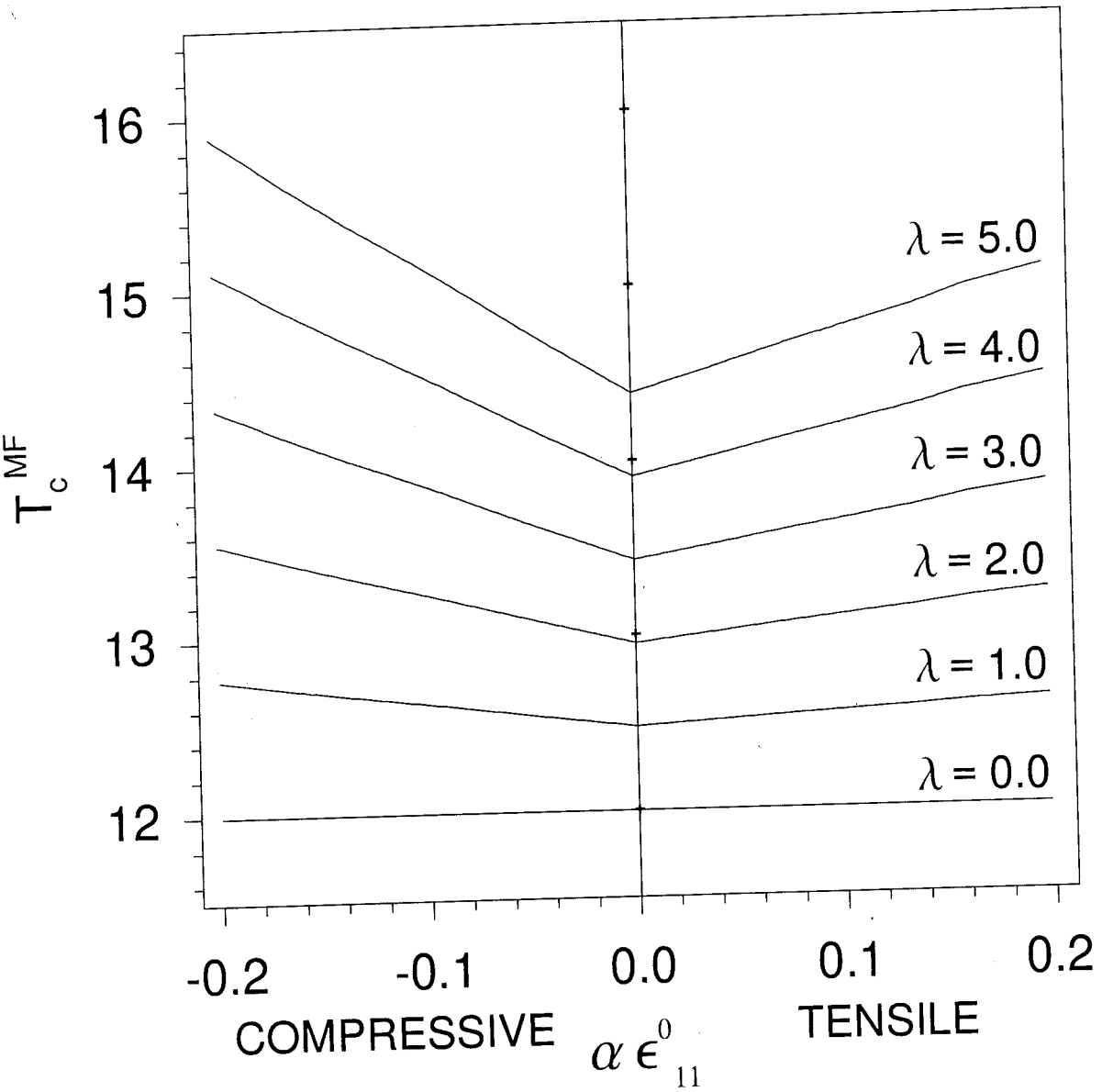
16
15
14
13
12
T_c^{MF}
$\lambda = 5.0$
$\lambda = 4.0$
$\lambda = 3.0$
$\lambda = 2.0$
$\lambda = 1.0$
$\lambda = 0.0$
-0.2
-0.1
0.0
0.1
0.2
COMPRESSIVE
TENSILE
$\alpha\, \epsilon^0_{11}$

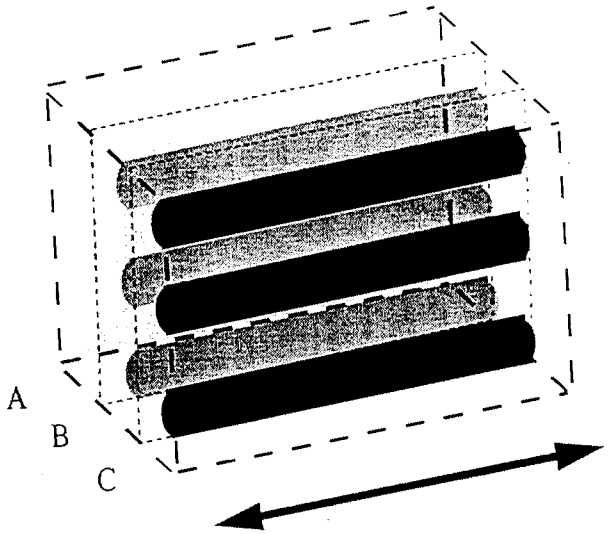

External Stress Axis

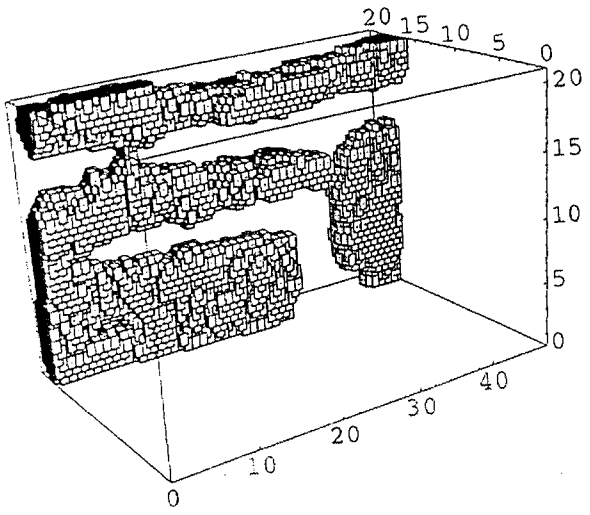

A

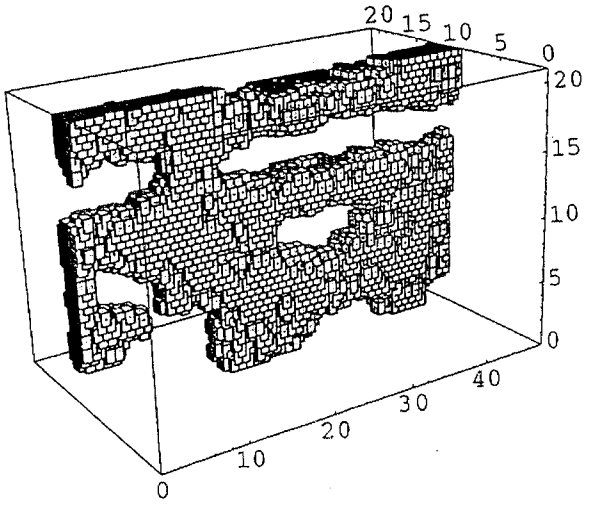

B

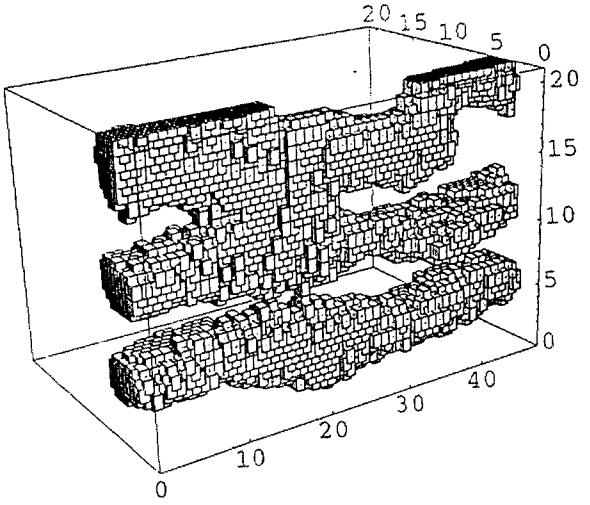

C

FIG. 3

FIG. 4

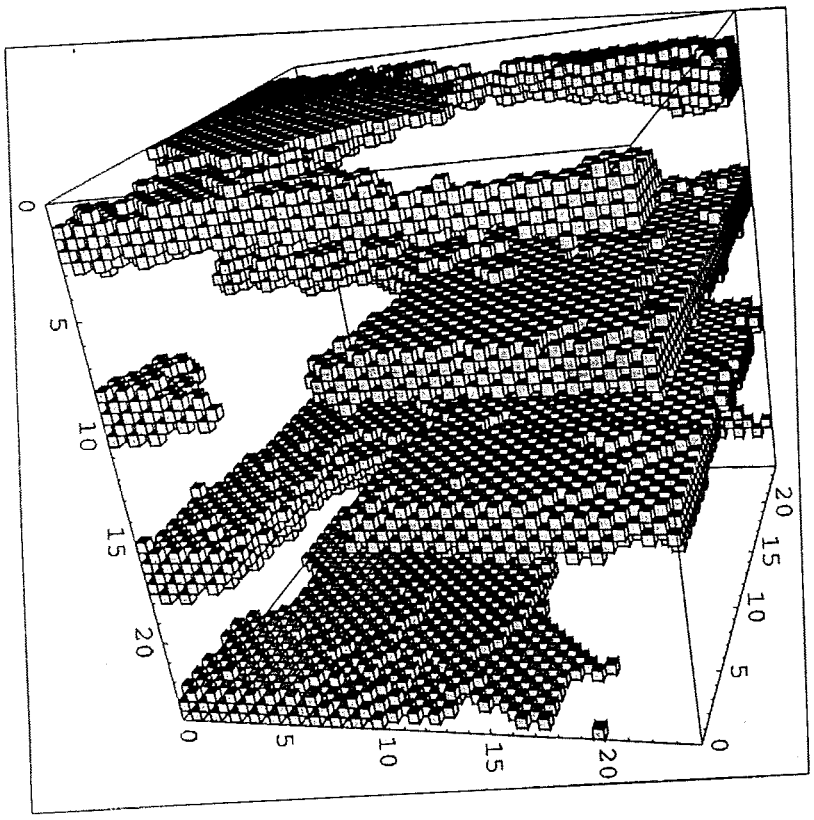
0
5
10
15
20
0
5
10
15
20

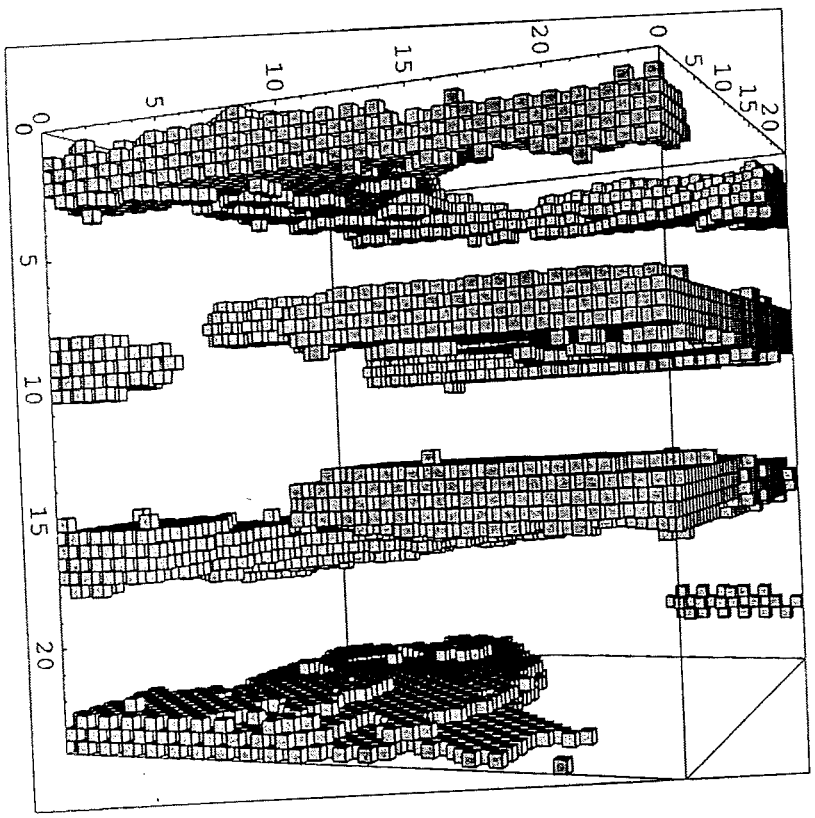
0
5
10
15
20
0
5
10
15
20

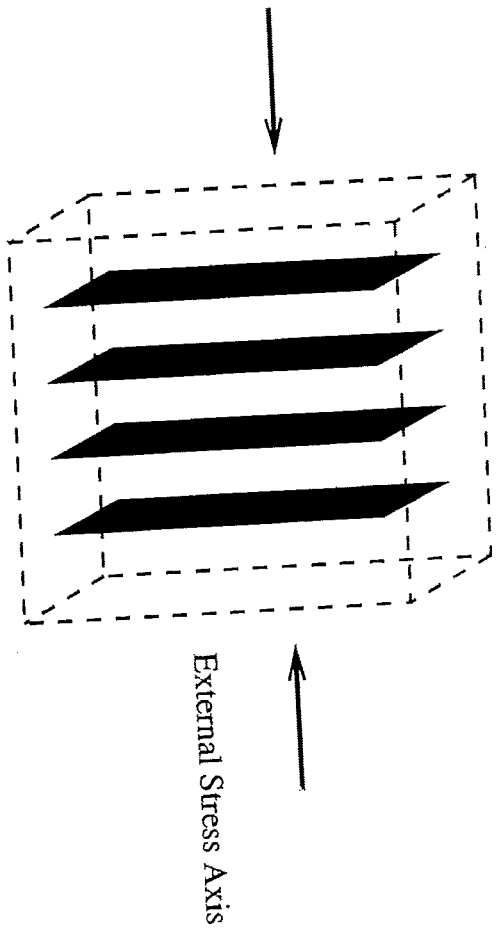
External Stress Axis

Uniaxial Stress Axis

Tensile

Compressive

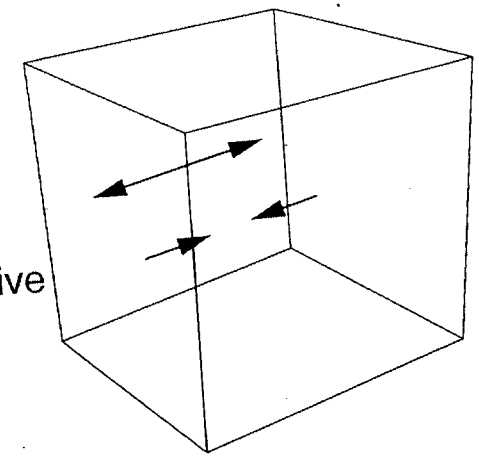

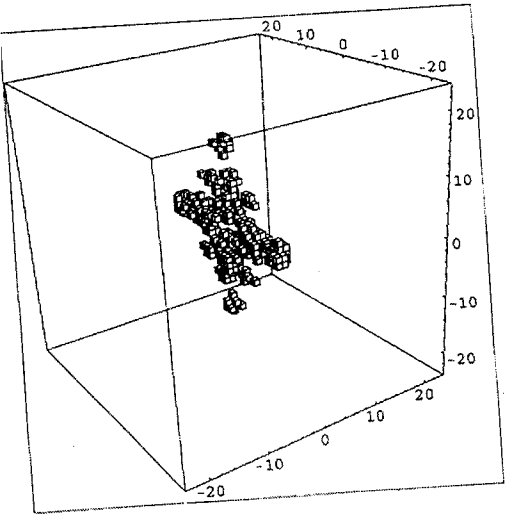

Tensile Stress

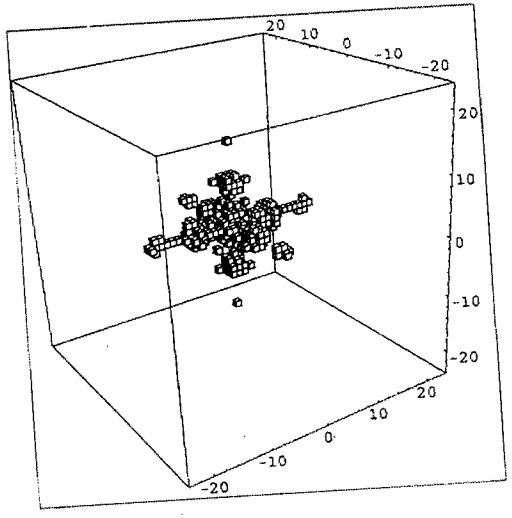

No Stress

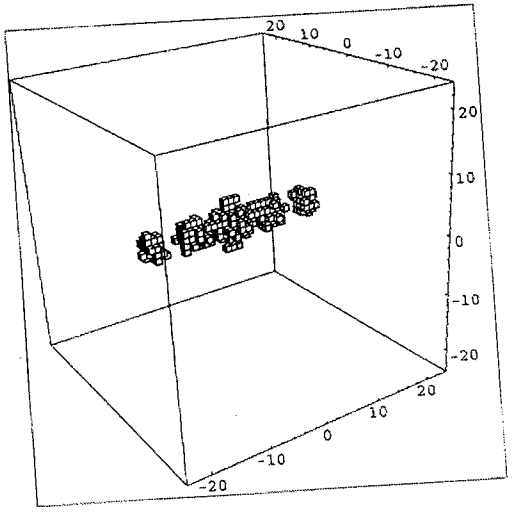

Compressive Stress

FIG. 5

FIG. 6

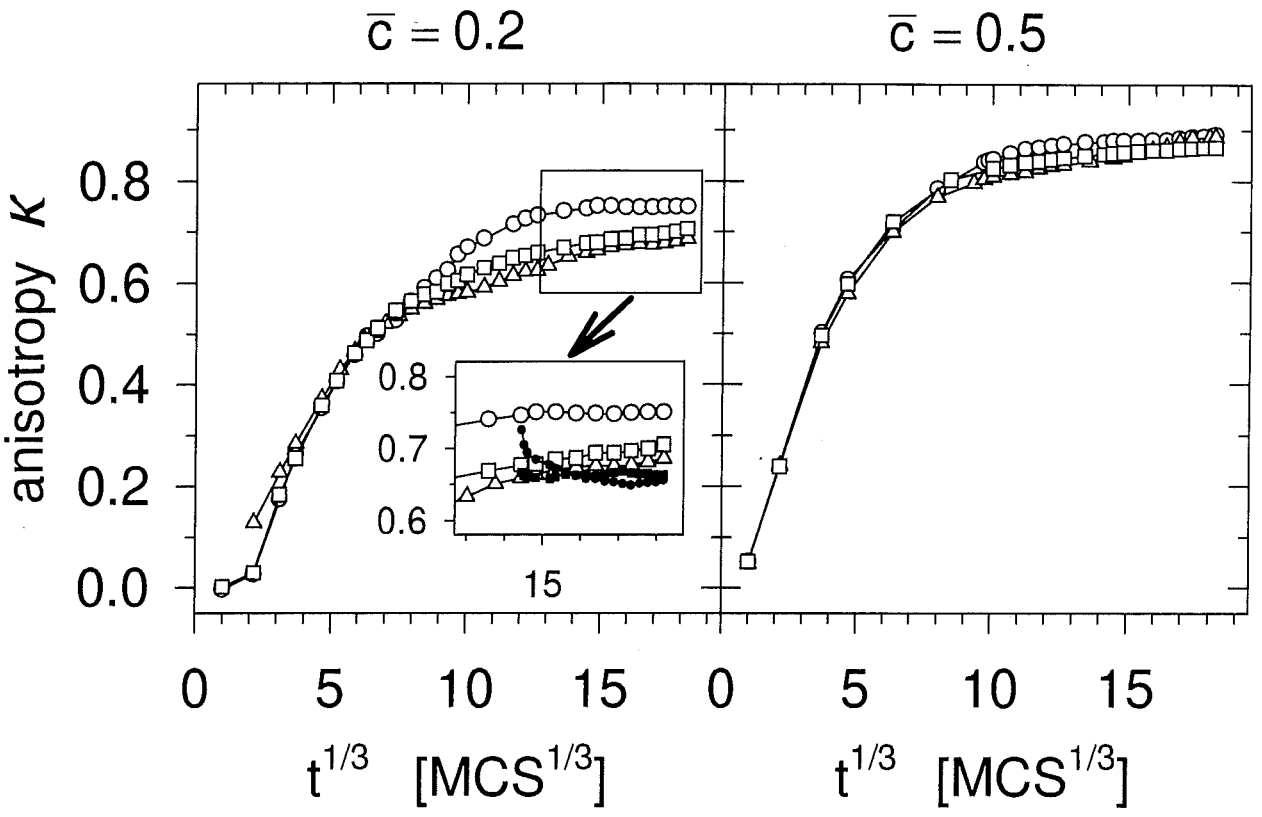
$\bar{c} = 0.2$
$\bar{c} = 0.5$
anisotropy K
0.0
0.2
0.4
0.6
0.8
0.6
0.7
0.8
15
0
5
10
15
$t^{1/3}$ [$MCS^{1/3}$]

FIG. 7

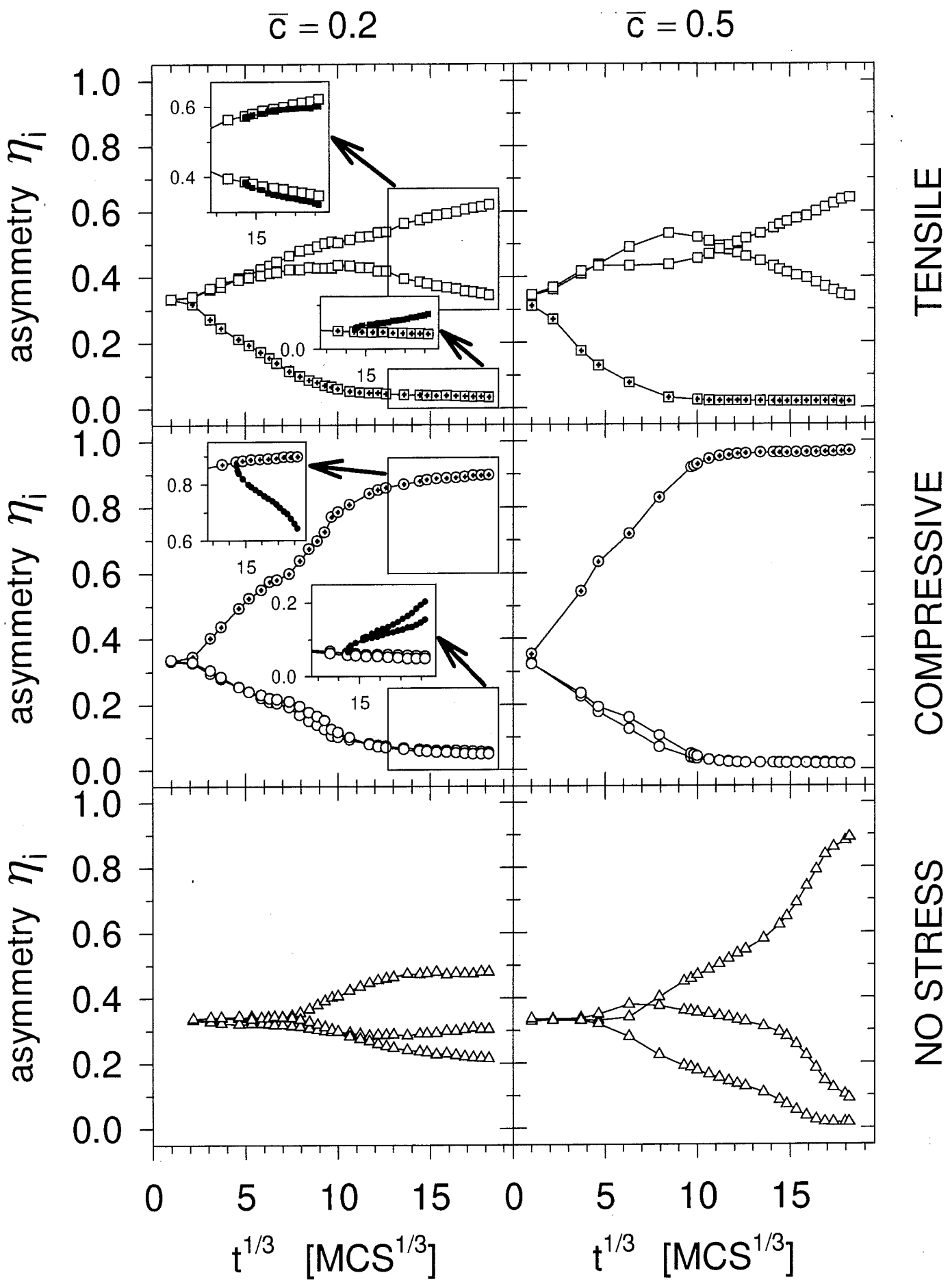
$\bar{c} = 0.2$
$\bar{c} = 0.5$
asymmetry η_i
TENSILE
COMPRESSIVE
NO STRESS
$t^{1/3}$ [$MCS^{1/3}$]
0
5
10
15
0.0
0.2
0.4
0.6
0.8
1.0

FIG. 8

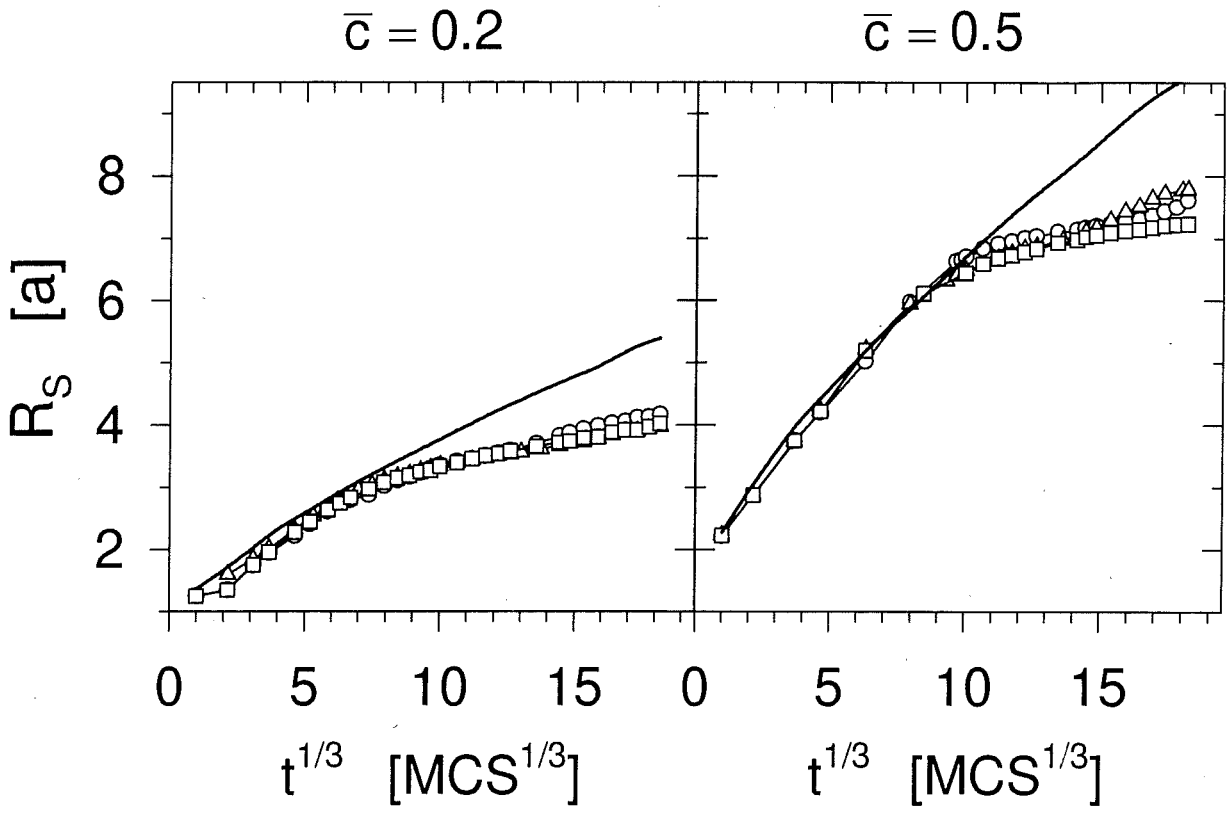

FIG. 9

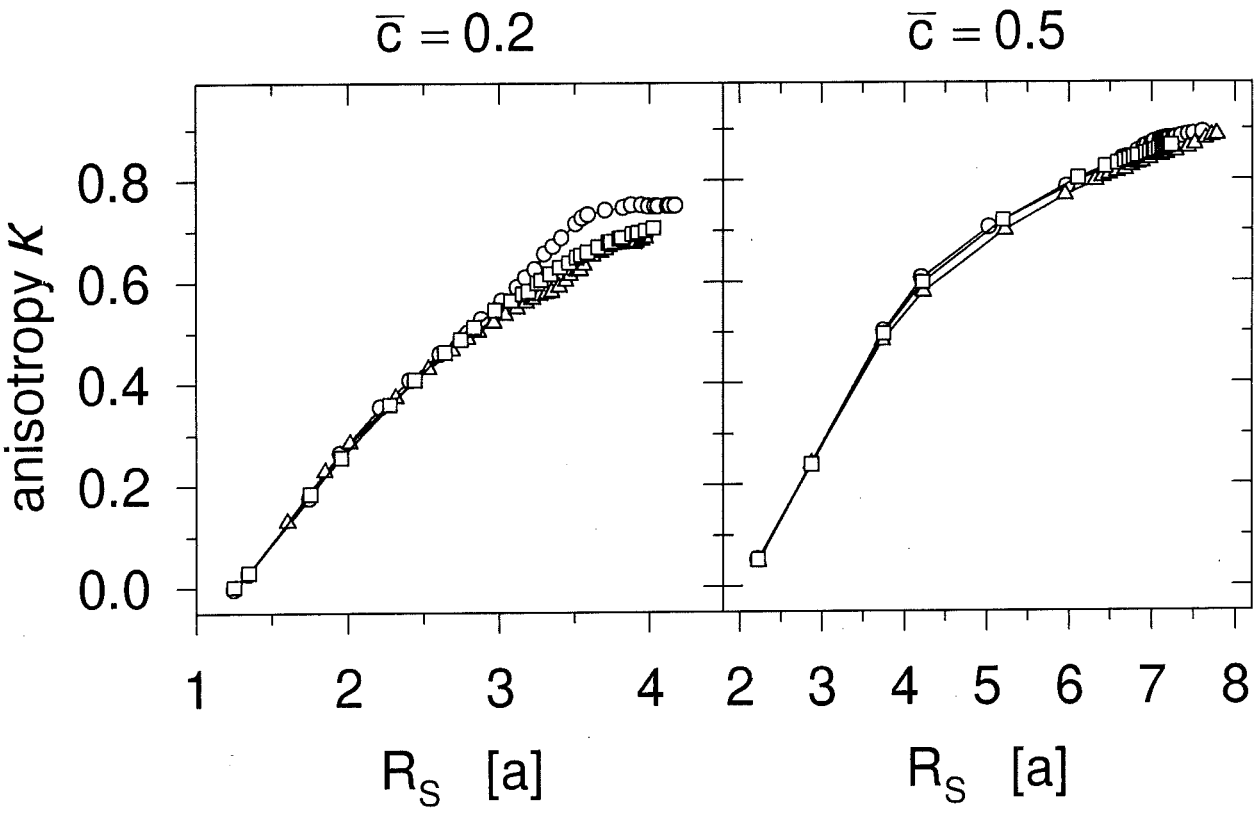
$\bar{c} = 0.2$
$\bar{c} = 0.5$
anisotropy K
0.0
0.2
0.4
0.6
0.8
1
2
3
4
2
3
4
5
6
7
8
R_S [a]
R_S [a]